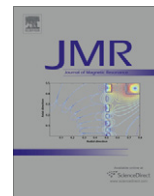




Contents lists available at ScienceDirect

Journal of Magnetic Resonance

journal homepage: www.elsevier.com/locate/jmr

Rapid measurement of transient velocity evolution using GERVAIS

Colin J. Davies^a, Andrew J. Sederman^a, Chris J. Pipe^b, Gareth H. McKinley^b,
Lynn F. Gladden^a, Mike L. Johns^{a,*}^aMagnetic Resonance Research Centre, Department of Chemical Engineering, University of Cambridge, Pembroke Street, Cambridge CB2 3RA, UK^bHatsopoulos Microfluids Laboratory, Department of Mechanical Engineering, Massachusetts Institute of Technology, Cambridge, MA 02139, USA

ARTICLE INFO

Article history:

Received 4 May 2009

Revised 28 September 2009

Available online xxxxx

Keywords:

Rheo-NMR

Transient velocity

EPI

Complex fluids

Velocimetry

ABSTRACT

Rapid velocity measurements using GERVAIS (Gradient Echo Rapid Velocity and Acceleration Imaging Sequence), an EPI (Echo Planar Imaging) based technique capable of measuring velocity over an observation time of several milliseconds, are performed on a wide-gap Couette Rheo-NMR cell for the first time. A variable delay time between a control signal to initiate a transition in flow and the start of the measurement sequence is incorporated to allow investigation of the transient evolution of the velocity field following a step change in rotation rate. Both the commencement and the cessation of imposed shear stress are investigated for (i) a shear banding micellar solution of CPyCl (cetylpyridiniumchloride)/NaSal (sodium salicylate) in brine and (ii) a low molecular weight PDMS (polydimethylsiloxane) oil. With respect to the micellar solution, an elastic shear wave is seen to propagate across the cell following the commencement of shear stress whilst an oscillatory 're-coil' is observed following the cessation of shear stress; neither of these phenomena were observed for the PDMS oil which exhibited a purely viscous response as expected for an incompressible Newtonian fluid. This technique has potential applications across a wide range of transient rheological investigations, particularly with respect to optically opaque materials.

© 2009 Published by Elsevier Inc.

1. Introduction

Fast MRI velocity measurements, capable of capturing transient flow effects, are of great interest in the study of fluid turbulence [1] and rheology [2]. Being able to visualize and understand rapid changes in the flow dynamics is useful, not only for comparison with modelling and simulations to validate transient flow solutions, but also for application to industrial systems, for example the transient flows of complex fluids used as cosmetic products [3,4]. It is thus desirable to measure velocity fields with a high temporal resolution to clearly resolve transient flow effects and flow instabilities with large growth rates. In this work, the GERVAIS (Gradient Echo Rapid Velocity and Acceleration Imaging Sequence) pulse sequence [5] was used to rapidly measure the transient evolution of velocity profiles within a wide-gap Couette cell.

The sample tested in this work is a shear banding micellar solution. Shear banding fluids demonstrate unusual rheological behaviour in that a pronounced stress plateau is seen in the 'flow curve' of stress versus shear rate [6]. This region of constant stress across a range of shear rates allows multi-banded strain rates across a constant stress flow. Shear banding fluids have recently been the

focus of much research using NMR methods ranging from bulk velocity measurements, which allowed the first direct visualisation of shear banding behaviour [7], to spectroscopy-based studies to understand the change in molecular orientations during shear [8]. Although investigations into the fluctuations seen in 'steady state' flows for this type of fluid have been conducted, no NMR-based measurements of the temporal velocity field response to step changes in imposed shear stress have been reported, to the best of our knowledge.

2. Background

One of the simplest approaches to speeding up traditional time-averaged 2D MRI velocity measurements is to replace the time-consuming phase encoding repetitions with an additional slice selective soft pulse e.g. [9,10]. Raynaud et al. [10] use a wide gap (inner and outer radii of 4 and 6 cm, respectively) Couette rheometer cell to investigate transient behaviour of a bentonite clay dispersion, with a temporal resolution of 25 s at a spatial resolution of 540 μm. A similar approach was adopted by Britton and Callaghan [11], who resolved the vertical velocity profile in a cone and plate rheometer cell at a spatial resolution of 23.4 μm with a total acquisition time of 15 s.

Holmes et al. and Lopez-Gonzalez et al. [12,13] were able to resolve the full propagator for each pixel at a resolution of 77 μm

* Corresponding author. Fax: +44 (0)1223 334796.

E-mail addresses: mlj21@cam.ac.uk, mlj21@cheng.cam.ac.uk (M.L. Johns).

across a 1 mm narrow gap Couette rheometer cell. Investigations using $\text{CPyCl}/\text{NaSal}$ micellar solutions were performed in experiments with times on the order of 5 h. Due to the time averaging technique employed, velocity variations on timescales shorter than the observation time were averaged out while velocity fluctuations on an intermediate time scale (i.e., shorter than the total experimental time) will manifest as blurring or multiple peaks in the measured propagators. Holmes et al. [12] were able to produce a remarkably accurate model of these spatially resolved propagators based on the corresponding measured shear stress fluctuations. In addition a 2D RARE velocimetry pulse sequence was used to monitor rapid variations in the radial 1D velocity field in the same Couette cell, at a spatial resolution of 100 μm , every 1 s. A series of 512 images were collected in order to study temporal fluctuations in the flow. At least two scans are required, however, for each velocity profile to 'restore' quadrature lost due to the addition of odd and even echoes [14,15].

3. Experimental

3.1. MRI pulse sequence details

EPI based pulse sequences to measure velocities rapidly have been developed based on both time-of-flight [16], and phase encoding [17] techniques. GERVAIS [5] is based on M-BEST (or blipped) EPI imaging with additional velocity encoding pulsed field gradients, separated by a refocusing 180° pulse, which serve to impart a phase shift proportional to velocity in the direction of the applied gradient; the pulse sequence is shown in Fig. 1. The magnetisation can be refocused to produce a series of velocity images; in the first image the velocity is calculated purely from the phase shift but subsequently it is calculated from the incremental phase shift between sequential images. Therefore no phase rewinding velocity gradients are required but a zero velocity image is used to correct for 'inherent' phase shifts in the absence of flow. GERVAIS has been used to image turbulent flow structures [5], flow fields in packed beds [18], flow in autocatalytic plumes [19], bubbly two-phase flow and flow in turbulent mixing cells.

With reference to Fig. 1, the delay time, τ , is defined as the delay between a control signal being sent from the Rheo-NMR motor and the application of the first velocity encoding gradient. For long delay times ($\tau > 10$ ms), the control signal was fired prior to the application of the initial 90° pulse; when this delay was shorter than 10 ms, the control signal was fired after application of the initial 90° pulse, thus splitting the echo pad delay (which is the time

required between the initial 90° pulse and the first 180° refocusing pulse to ensure that the resultant echo occurs at the centre of k -space). Thus a number of delay times, τ , between the commencement or cessation of shear and velocity encoding over Δ were investigated using separate experiments. Each measurement was repeated eight times and an average was taken.

An initial EPI image was acquired using a pixel raster of 64 × 32 pixels which gave a spatial resolution of 312 μm × 625 μm per pixel. Subsequent applications of GERVAIS typically used a velocity encoding gradient application time of $\delta = 1$ ms and an observation time of $\Delta = 3.1$ ms. The gradient strength was selected to ensure that a broad range of phase shifts were achieved. Sequences of four successive images were acquired off a single excitation for all samples, but frequently it was found that later images had poor signal-to-noise ratios and were discarded. For each fluid sample the recovery time between successive shear commencement experiments was several minutes to ensure that the fluid microstructure was fully equilibrated and residual stresses had decayed. Similarly in the cessation of steady shear flow experiments the sample was sheared for several (typically 10) minutes at a steady rate to ensure it was at steady state. In all cases, a zero velocity reference signal was subtracted from the experimental results to remove intrinsic phase changes.

All experiments were performed using a Bruker DMX 300 employing a 7.14 T vertical-bore superconducting magnet and a 25 mm i.d. r.f. coil.

3.2. Rheo-NMR

The basic (Bruker) Rheo-NMR kit used is that described by Callaghan [20], from whom it was purchased and which we have used previously to study emulsion rheology [21]. It allows standard rheological cells to be inserted into the imaging region of a magnet to enable non-invasive imaging of fluids under controlled shear. The cells are attached to, and rotated by, a drive shaft (powered by an external motor sitting in the stray field at the top of the magnet) that is inserted into the magnet bore. The motor is attached to a motor-drive controller, distant to the magnet, used to control the speed and direction of rotation; this is connected to the spectrometer to allow control of the motor during the execution of imaging pulse sequences. In the current rheological application, a wide-gap Couette cell is used, constructed from PEEK (Polyetheretherketone) with inner and outer radii of $r_i = 6.0$ mm and $r_o = 9.0$ mm, respectively, giving a gap ratio $d = (r_o - r_i)/r_i = 0.5$. The surface of the inner cylinder wall was knurled to reduce wall slip. The inner cylinder was hollow and was filled with a marker fluid which experiences a solid body rotation whilst the cell is being rotated.

A modification to the standard Bruker Rheo-NMR set-up was required as the motor is initially programmed to ramp up to the desired speed slowly over the timescale of several seconds. The desired rotational speed setting is transmitted via a logic port on the spectrometer to the motor control unit to allow integration of motor control into pulse programs. The counter used to set the speed is incremented on the downward stroke of a square wave input; as this is ramped up the motor follows the input in real time and the rotation rate gradually increases. A second control line is used to reset the counter and hence turn the motor off. An alternative control arrangement, with an additional input, was implemented. The new design incorporates three control lines: increment, reset and, in addition, a new motor enable line. The control unit accepts a similar square wave signal to increment the counter and, if desired, this can be set to zero using the reset line. However, in contrast to the previous configuration, changing the counter will not affect the motor until a positive signal is sent on the motor enable control line. When this is set high, the stepper

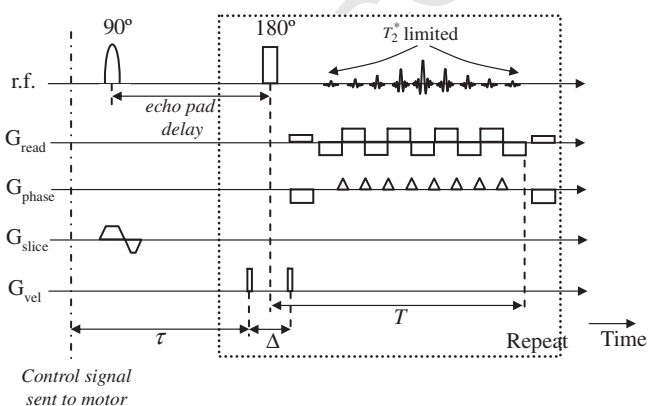


Fig. 1. GERVAIS pulse sequence. Velocity encoding takes place over the observation time Δ , whilst spatial resolution into an image occurs over T . The delay between the control signal being sent to the motor (for cessation/commencement of steady shearing) and the application of the first velocity encoding gradient, τ , is also shown.

188 motor will be activated. The major benefit is that instead of the
189 system response time being dominated by the control signal delays
190 and the motor taking several seconds to reach full speed, its re-
191 sponse curve will more closely resemble a step function.

192 3.3. Experimental details

193 The sample being considered in this study is a 0.1 M cetylpyri-
194 dinium chloride (CPyCl)/0.05 M sodium salicylate (NaSal) in 0.1 M
195 NaCl aqueous solution. Similar micellar systems have already been
196 extensively studied in shear and extensional flow (e.g. [22,23]). The
197 sample was prepared using the method described in [24]; the brine
198 solution was created by heating 500 mL deionized water to 30 °C
199 and adding 2.922 g NaCl whilst the solution was stirred. CPyCl
200 (17 g) was added followed by the slow addition of 4 g of sodium
201 salicylate. The stirring was continued to allow all trapped air bub-
202 bles to rise out of the solution. For comparison purposes, all mea-
203 surements were repeated using a Newtonian 100 cSt PDMS
204 solution (molecular weight 6250 g/mol, purchased from Sigma-
205 Aldrich). Table 1 provides an overview of the material properties for
206 the test fluids. For the CPyCl/NaSal solution, water was used as the
207 marker fluid in the centre of the Couette cell; for the PDMS mea-
208 surements, water was replaced with additional PDMS to eliminate
209 chemical shift artefacts.

210 Both the commencement and cessation of steady shear flow
211 experiments used a rotation rate $\Omega_0 = 1.4 \text{ rad s}^{-1}$ of the inner cyl-
212 inder. For a Newtonian fluid the steady-state velocity $u(r)$ and
213 shear rate $\dot{\gamma}(r)$ profiles in a cylindrical Couette device are given by:

$$215 \quad u = \frac{\Omega_0 r_i}{r_o/r_i - r_i/r_o} \left[\frac{r_o}{r} - \frac{r}{r_o} \right], \quad (1a)$$

$$217 \quad \dot{\gamma}_i = \frac{dv}{dr} = \frac{-\Omega_0 r_i}{r_o/r_i - r_i/r_o} \left[\frac{r_o}{r^2} + \frac{1}{r_o} \right]. \quad (1b)$$

218 Thus the magnitude of the shear rates at the inner and outer
219 walls are $\dot{\gamma}_i = 3.64 \text{ s}^{-1}$ and $\dot{\gamma}_o = 2.24 \text{ s}^{-1}$, respectively. For conven-
220 ience we shall refer to the nominal shear rate acting in the Cou-
221 ette cell based on the small gap approximation $d \ll 1$, and
222 defined as $\dot{\gamma}_{\text{nominal}} = \Omega_0/d = 2.8 \text{ s}^{-1}$. This gives a nominal Weiss-
223 enberg number $Wi = \dot{\gamma}_{\text{nominal}} \cdot \lambda = 0.98$ (λ is the material viscoelas-
224 tic relaxation parameter) and indicates that the experiments are
225 conducted where viscoelastic effects are important but before the
226 onset of shear banded flow [25]. This is convenient as it allows
227 us to investigate viscoelastic flow with the CPyCl/NaSal solution
228 independently of shear banding.

229 4. Theory

230 The wide-gap Couette cell used in these measurements has an
231 inner cavity which is filled with a Newtonian marker fluid. The
232 transient evolution of the velocity field for a Newtonian fluid fol-
233 lowing the commencement of steady shear can be solved analyt-
234 ically [26]. The solution is thus the time-dependent velocity
235 profile (in the direction of superficial flow) as a function of radial

Table 1

Test fluid properties at 25 °C. The values indicated for the viscoelastic relaxation time and elastic modulus of the CPyCl/NaSal solution are those found previously for an identical system in [24].

| Fluid | Viscosity, η (Pa s) | Density, ρ (kg/m ³) | Elastic modulus G_0^N (Pa) | Relaxation time τ (s) |
|-------------|-----------------------------|---|---------------------------------|-------------------------------|
| CPyCl/NaSal | 7.8 | 1045 | 22.4 | 0.35 |
| PDMS | 9.7×10^{-2} | 970 | – | – |
| Water | 8.9×10^{-4} | 997 | – | – |

236 position $u(r, t)$ within a hollow cylinder (of radius a) initially at rest
237 being subjected to a step change in angular frequency.

238 By equating the rate of change of angular momentum of the
239 fluid in a cylindrical shell (per unit length and thickness) to the
240 couple acting on it, it can be shown that:

$$242 \quad \frac{\partial u}{\partial t} = \nu \left(\frac{\partial^2 u}{\partial r^2} + \frac{1}{r} \frac{\partial u}{\partial r} - \frac{u}{r^2} \right). \quad (2)$$

243 ν is kinematic viscosity. The relevant initial and boundary condi-
244 tions are:

$$245 \quad u(r, 0) = 0 \quad \text{for } 0 \leq r \leq a \quad (3)$$

$$246 \quad u(a, t) = \Omega_0 a \quad \text{for } t > 0. \quad (4)$$

247 where Ω_0 is the steady state angular rotation rate. From this, the
248 time-dependent velocity distribution can be found as:

$$249 \quad u(r, t) = \Omega_0 r + 2\Omega_0 a \sum_{n=1}^{\infty} \frac{J_1(\lambda_n \frac{r}{a})}{\lambda_n J_0(\lambda_n)} \exp\left(-\lambda_n^2 \frac{\nu t}{a^2}\right), \quad (5)$$

252 where J_0 and J_1 are Bessel functions of the first kind of order zero
253 and one, respectively, and λ_n are the positive roots of $J_1(\lambda) = 0$.

254 We also give the solutions for transient flow in a planar Couette
255 geometry which will be used to approximate the time-dependent
256 flow in the Couette device:

$$257 \quad \frac{u}{u_0} = 1 - \left(\frac{y}{b}\right) - \sum_{n=1}^{\infty} \left(\frac{2}{n\pi}\right) \sin\left(\frac{n\pi y}{b}\right) \exp\left(-n^2 \pi^2 \frac{\nu t}{b^2}\right). \quad (6a)$$

$$260 \quad \frac{u}{u_0} = \sum_{n=1}^{\infty} \left(\frac{2}{n\pi}\right) \sin\left(\frac{n\pi y}{b}\right) \exp\left(-n^2 \pi^2 \frac{\nu t}{b^2}\right), \quad (6b)$$

263 where $u_0 = \Omega_0 r_i$ and $b = r_o - r_i$ and the approximate transient solu-
264 tions for start-up and cessation of steady shearing flow (following
265 an impulse change) are given by Eqs. 6(a) and (b), respectively.
266 For this planar approximation, the Cartesian coordinate y is equiv-
267 alent to the radial coordinate r in the cylindrical coordinate system.

268 5. Results

269 5.1. Validation with time averaged techniques

270 A comparison of GERVAIS with a traditional spin-echo 2D veloc-
271 ity map measurement (requiring 28 min to acquire) is presented in
272 Fig. 2 for the CPyCl/NaSal solution in the Couette cell at steady
273 state at a nominal shear rate of 2.8 s^{-1} . Fig. 2(a) is the GERVAIS
274 velocity image where the velocity component in the vertical direc-
275 tion in the figure has been measured (the black arrows indicate the
276 direction of rotation). The CPyCl/NaSal solution resides in the
277 annular cell with water present as a marker fluid in the central
278 chamber. The white box in Fig. 2(a) indicates the slice extracted
279 for all subsequent velocity profile data. Here the azimuthal velocity
280 component is parallel to the phase imaging gradient. In this slice
281 (and only in this slice) a complete description of the rotating fluid's
282 velocity in the transverse plane can be found by measuring a single
283 (in this figure vertical) component of velocity. This slice has been
284 extracted and is presented in Fig. 2(b) for both the conventional
285 time averaged and the GERVAIS measurement. Good agreement
286 is found between the two measurements, however, the left hand
287 side (LHS) of the GERVAIS profile presents slightly poorer agree-
288 ment. This highlights the sensitivity of EPI based techniques to
289 shimming quality; a slightly poorer shim in this region has resulted
290 in slightly erroneously high velocity values being measured.

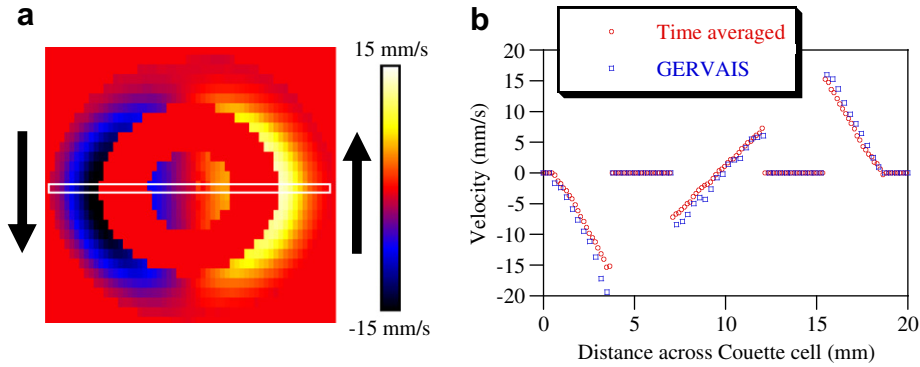


Fig. 2. (a) Image of one component of velocity for flow of CPyCl/NaSal solution in the wide-gap Couette cell measured using GERVais. (b) The data from the white rectangle has been extracted and compared to a time-averaged spin echo based technique.

5.2. Start-up steady shear flow

Velocity profiles across the Couette cell for the CPyCl/NaSal solution for a variety of delays, τ , between starting the motor and application of the velocity encoding gradients are shown in Fig. 3. Over the first few milliseconds, the CPyCl/NaSal fluid in the annular gap starts to approach the speed of the inner wall as would be expected. However, from 7.2 ms onwards, a velocity wave can be seen to propagate across the cell with the highest velocity no longer evident at the inner wall. In fact this highest velocity significantly exceeds that of the inner wall. This elastic shear wave consisting of fluid flowing at a comparatively high velocity, is seen to cover a large portion of the cell gap at a delay of 19.5 ms. The fluid velocity overshoots then relaxes back into the steady state after ~ 100 ms. The elastic wave is similar to that observed by Miller and Rothstein [23] for the same CPyCl/NaSal solution in a Couette geometry (albeit for a narrower non-dimensional gap $d = 0.08$) using particle imaging velocimetry (PIV). The

steady state viscoelastic velocity profile is attained after approximately 0.5 s and we note the absence of visible shear bands. This is in good agreement with the results of Miller and Rothstein [25] where significantly shear banded flow was not observed before a non-dimensional shear rate $Wi = 8.4$, which is an order of magnitude greater than the value in the present work $Wi = 0.98$. The water in the centre takes longer (approximately 5 s) to reach its steady-state velocity, as expected due to its lower viscosity.

The standard error, SE, between repeat measurements has been calculated as

$$SE = \frac{s}{\sqrt{n}}, \quad (7)$$

where s is the standard deviation across the n (in this case $n = 8$) measurements taken for every pixel across the Couette cell gap for every delay time used. The standard error has been averaged across both of these dimensions (time delay and spatial position

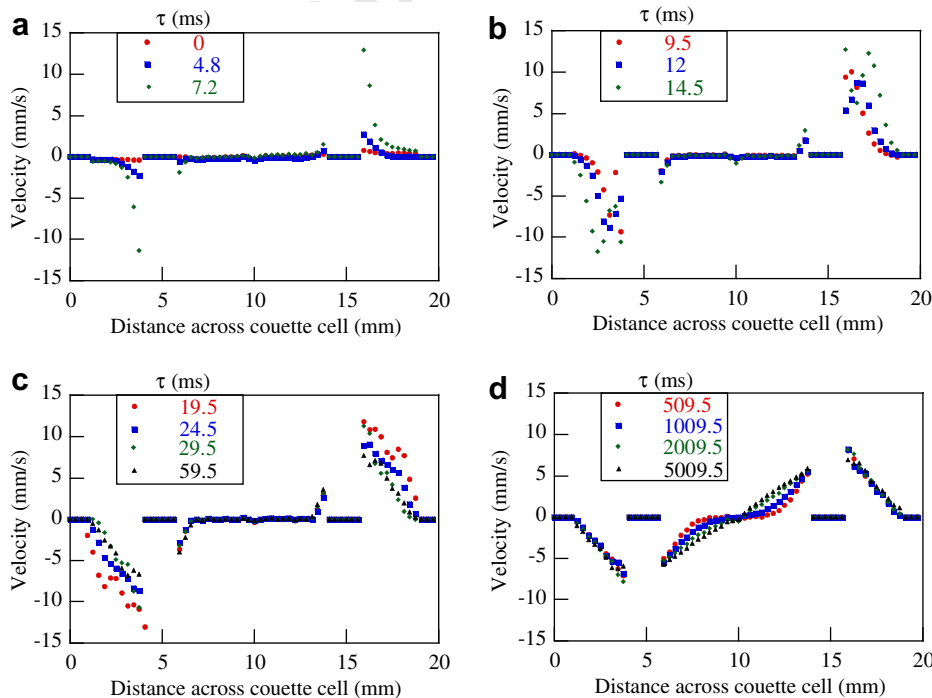


Fig. 3. Velocity profiles of the initial start-up flow in a Couette cell acquired using GERVais with delays of (a) 0, 4.8 and 7.2 ms; (b) 9.5, 12 and 14.5 ms; (c) 19.5, 24.5, 29.5 and 59.5 ms; (d) 509.5, 1009.5, 2009.5 and 5009.5 ms after commencement of shear with a nominal shear rate $\dot{\gamma}_{nominal} = 2.8 \text{ s}^{-1}$. The inner cavity contains water and the outer cavity contains the CPyCl/NaSal solution.

across the Couette gap) and was calculated as ± 0.2 mm/s, which is less than the symbol size used in Fig. 3.

The data in Fig. 3 can be compared to the corresponding results for a viscous PDMS oil shown in Fig. 4. A steady increase in the velocity profile is observed with no elastic wave present. After ~ 20 ms the flow field essentially reaches its steady state profile. This confirms that the elastic wave observed in the CPyCl/NaSal solution is not an artefact of the Rheo-NMR cell or the pulse sequence implementation. The inner marker fluid (PDMS) is seen to approach its steady-state velocity in a much shorter timescale (around 2 orders of magnitude less) than the water in Fig. 3, as expected. The results for the Newtonian PDMS and water are in reasonably good agreement with predictions for the transient velocity field for a viscous fluid both inside the central cavity and the cylindrical Couette cell (shown by the solid lines), as predicted by Eqs. (5) and (6a), respectively. This can also be seen by comparing the velocity measurements shown on a 2D space-time plot in Fig. 5 with the theoretical predictions from Eqs. (5) and (6). Such a good level of agreement between the predicted velocity profiles and the corresponding experimental data strongly suggests that the assumption of an approximate step function for the commencement of shear is valid. It is also a clear indication that the characteristic time of the impulsively started motor is much smaller than the characteristic viscous diffusion time of the liquid and the flow undergoes an approximate step change in shear rate as required.

5.3. Cessation of steady shear flow

The natural complement to measuring fluid response to a step increase (from zero) of average shear rate is the investigation of the response to an abrupt cessation of shearing. Fig. 6 shows velocity profiles for a series of delay times, τ , following the cessation of steady shear for the CPyCl/NaSal solution. At short delays (< 10 ms) the fluid decelerates as expected. This deceleration preferentially occurs closer to the inner stationary wall. The direction of flow then reverses so that, after 14.5 ms, the fluid is rotating in the opposite (negative) direction. The water in the inner cavity continues to rotate in the direction of initial shearing due to inertia, showing that this local flow reversal is not an experimental artefact but a consequence of fluid viscoelasticity. The fluid in the outer cavity then rebounds to flow in the original direction again, with a local peak in mean velocity magnitude occurring approximately 40 ms after the cessation of imposed shear. The water in the central cavity continues to rotate in the initial direction (as expected due to its lower viscosity) and only comes to a complete stop in excess of 1 s after the cessation of shear. Fig. 7 shows the corresponding shear cessation data for PDMS. The fluid motion decays monotonically as expected; no flow recoil and velocity rebound is observed as with the CPyCl/NaSal solution. This thus provides

further supporting evidence that the velocity response for the CPyCl/NaSal solution, observed in Fig. 6, is not an artefact of the equipment or pulse sequence implementation. Additionally, examining the velocity data near the inner wall in Fig. 7 reveals the finite stopping time of the rotating inner cylinder; note that this is not consistent with the approximate analytical solution (shown by the solid lines) which predicts a zero velocity at the inner wall. The rotation rate $\Omega(t) = \Omega_0 \exp(-t/t_c)$ of the inner cylinder during cessation of flow is well described by $\Omega(t) = \Omega_0 \exp(-t/t_c)$, where the time-constant $t_c \approx 3.6$ ms. Preliminary investigations suggest that the ~ 1 m long aluminium drive shaft and its assembly to the motor and the rheo-cell are the primary causes for this non-ideal transition; this will be quantified in future work. After only 10 ms, however, the inner cylinder is effectively at rest, providing a reasonable approximation of impulsively stopped flow for this experimental configuration.

The data from Figs. 6 and 7 is presented as a 2D plot in Fig. 8, where the elastic recoil, observed for the CPyCl/NaSal solution, is distinctly evident. Note that the transition to flow in a reverse direction occurs first adjacent to the inner rotating wall, where the original shear rate and hence elastic stresses are largest.

5.4. Theoretical comparison

Lee and Fuller [27] investigated the transient response of viscoelastic polystyrene-tricresyl phosphate solutions in a cylindrical Couette set-up after step increases in the applied shear rate. The point-wise time evolution of the shear stress was monitored using flow birefringence and allowed the local elastic shear wave speed to be calculated. The measured shear wave speed c was in good agreement with the theoretical value predicted by Joseph [28]:

$$c = (G_0^N / \rho)^{1/2}, \quad (8)$$

where G_0^N is elastic modulus and ρ is fluid density. Analogously, in Fig. 9 we extract the maximum velocity in each profile for the CPyCl/NaSal measurements for both sides of the Couette cell from Fig. 6 and plot these against the delay times to measure the oscillation and the damping of the fluid motion. These data were fitted to an exponentially damped sinusoidal oscillation described by:

$$u = u_0 \cos\left(\frac{2\pi}{b}t\right) \exp\left(-\frac{t}{c'}\right), \quad (9)$$

where u is velocity, u_0 the initial velocity, t is time and b and c' are the period and damping time-constant, respectively. The fitting parameters were found to be $c' = 25$ ms and $b = 41$ ms. For impulsively started/stopped planar Couette flow of a Maxwell fluid, Denn and Porteous [29] derive an analytical form of the transient velocity field. This gives the period of the dominant oscillatory mode and the damping time-constant to be:

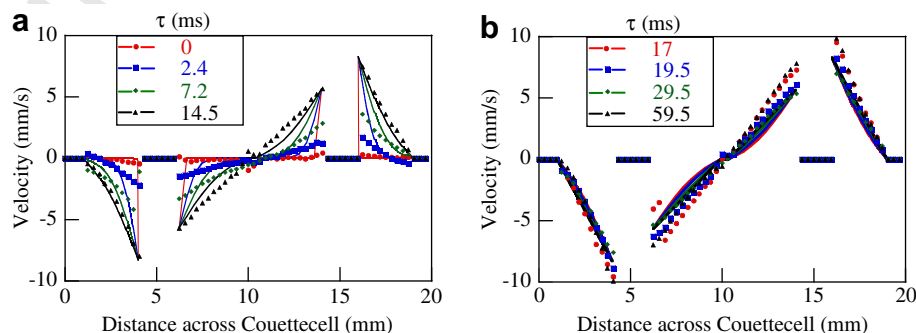


Fig. 4. Velocity profiles of the start-up flow in a Couette cell acquired using GERVAIS with delays of (a) 0, 2.4, 7.2 and 14.5 ms and (b) 17, 19.5, 29.5 and 59.5 ms after commencement of steady shear. The inner and outer cavities both contain PDMS. The analytical velocity profiles given by Eq. (6a) are shown as solid lines for comparison.

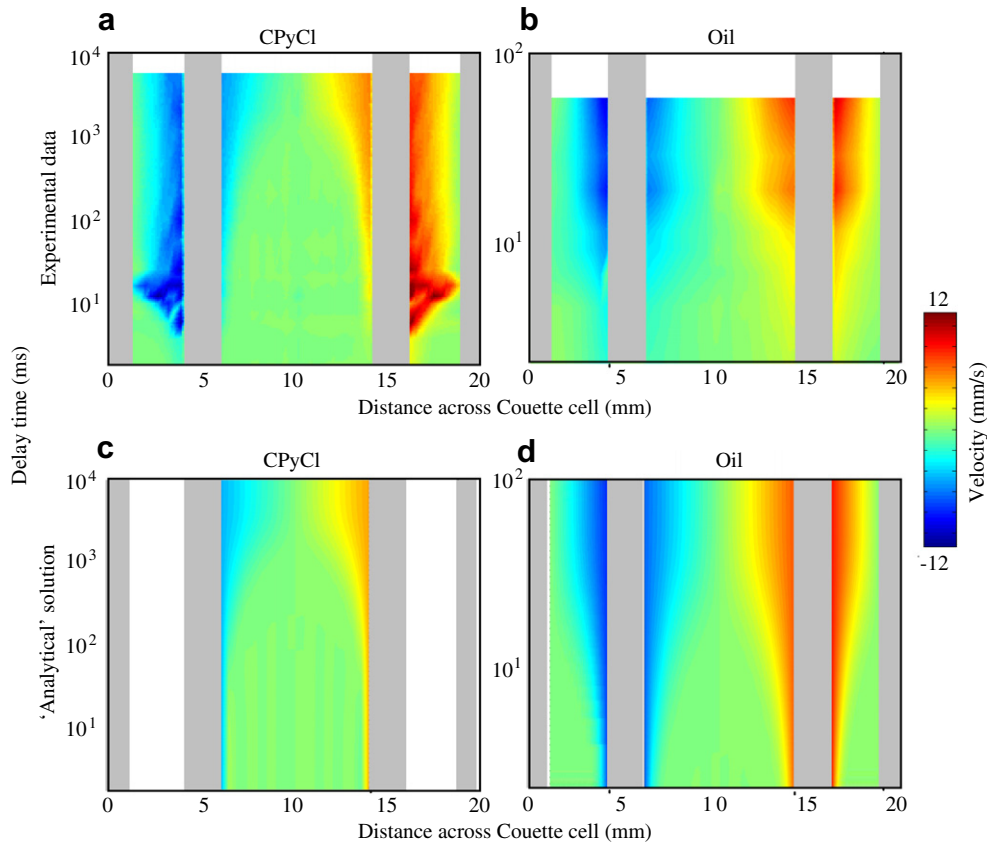


Fig. 5. 2D velocity (shown using colour scale) plots with profile position and time as axes for (a) CPyCl/NaSal solution (data from Fig. 3) and (b) PDMS sample (data from Fig. 4) for the start up experiments. The evolution of the velocity profile in time can be seen more clearly. Analytical solutions (Eq. (5)) for comparison for the Newtonian marker fluids in the central cavity for this start-up flow are shown in (c) for water (where the CPyCl/NaSal is in the outer cavity) and (d) PDMS, where the approximate analytical response for flow in the Couette cell is also shown (Eq. (6a)). A perfect step function response was assumed.

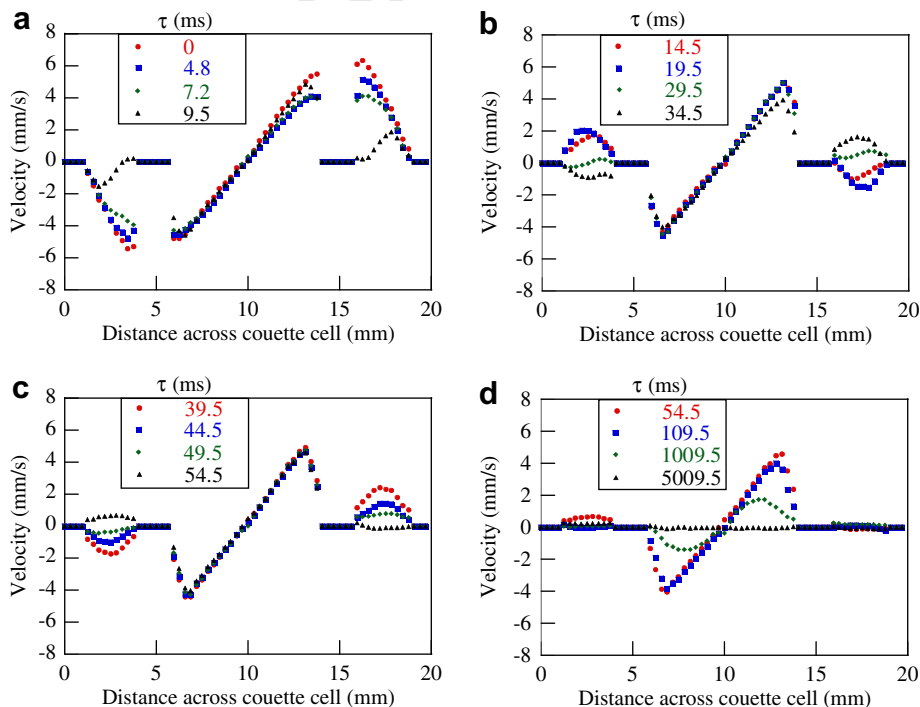


Fig. 6. Velocity images of the stopping flow in a Couette cell acquired using GERVAIS with delays of (a) 0, 4.8, 7.2 and 9.5 ms; (b) 14.5, 19.5, 29.5 and 34.5 ms; (c) 39.5, 44.5, 49.5 and 54.5 ms; (d) 54.5, 109.5, 1009.5 and 5009.5 ms after the cessation of shear. The inner cavity contains water and the outer annulus contains CPyCl/NaSal solution.

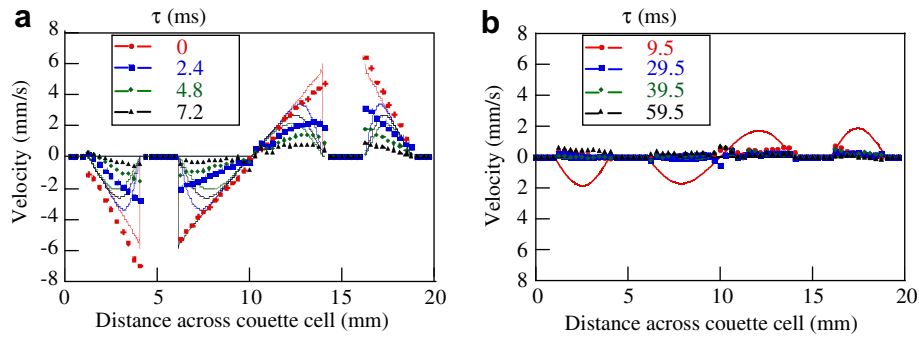


Fig. 7. Velocity images of stopping flow in a Couette cell acquired using GERVAIS with delays of a) 0, 2.4, 4.8 and 7.2 ms and b) 9.5, 29.5, 39.5 and 59.5 ms after the cessation of steady shear flow. The inner and outer cavities both contain PDMS. Results for the analytical transient velocity profiles (Eqs. (5) and (6b)) are shown as solid lines for comparison.

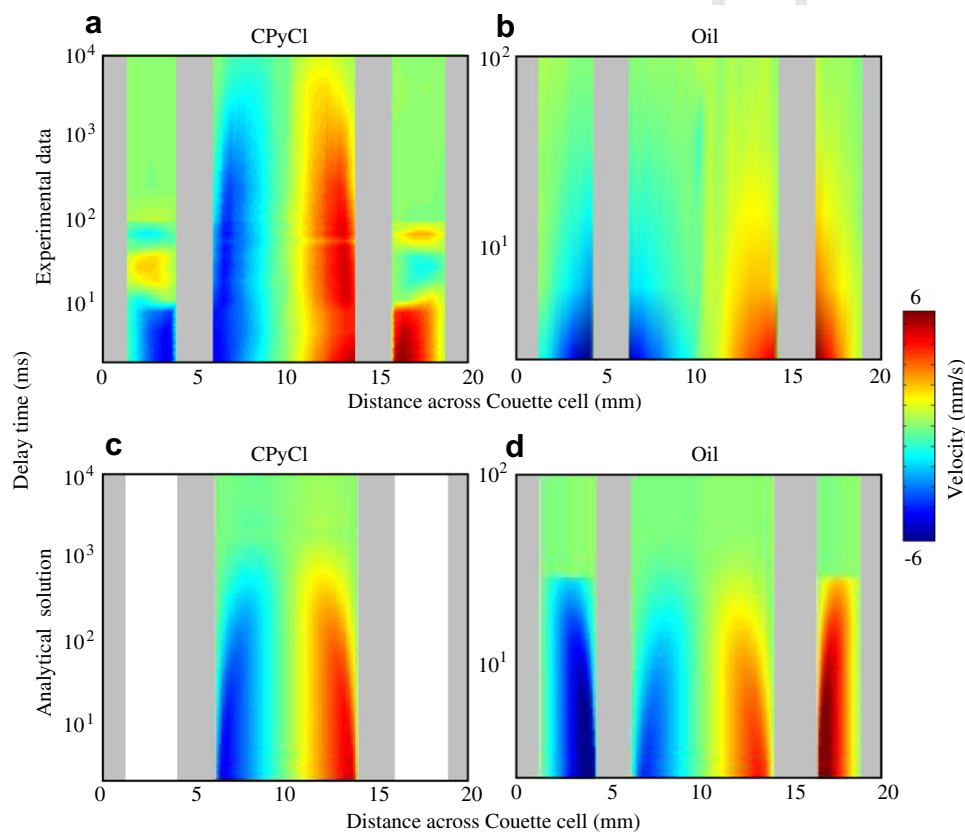


Fig. 8. 2D velocity (shown using colour scale) plots with profile position and time as axes for (a) CPyCl/NaSal solution (data from Fig. 6) and (b) PDMS sample (data from Fig. 7) for the stopping experiments. Analytical solutions (Eq. (5)) for comparison to the Newtonian marker fluids in the central cavity for this stopping flow are shown in (c) for water (where the CPyCl/NaSal is in the outer cavity) and (d) PDMS, where the approximate analytical response for flow in the Couette cell is also shown (Eq. (6b)).

$$b = \frac{4\pi\tau}{\sqrt{4\pi^2El - 1}}, \quad (10a)$$

$$c' = 2\tau, \quad (10b)$$

for $El > 1$ and where the elasticity number $El = \eta\lambda/(\rho d^2)$. From Eq. (10a) the period of the elastic shear wave b is calculated to be 41 ms, in excellent agreement with the value measured in the Couette cell. The viscoelastic damping coefficient, however, is significantly over-estimated in Eq. (10b) which predicts $c' = 700$ ms. This could be due to the finite stopping time of the rotating inner cylinder affecting the viscoelastic damping (the time-constant for the slowing inner cylinder $tc \approx 3.6$ ms is of the same order as the timescale of viscous diffusion for the micellar network $d^2\rho/$

$\eta = 1.2$ ms). Furthermore, the nominal Weissenberg number $Wi = 0.98$ suggests that non-linear viscoelasticity may be responsible for the stronger damping observed in the micellar network compared to that expected for a linear Maxwell fluid.

6. Discussion

The use of a delay time in combination with the GERVAIS pulse sequence enables the temporal evolution in velocity fields to be imaged following a change in imposed shear stress. Velocity encoding occurs over a time Δ (where $\Delta = 3.1$ ms in our implementation) and thus velocity fluctuations over time scales less than this will not be resolved. The application of imaging gradients (read

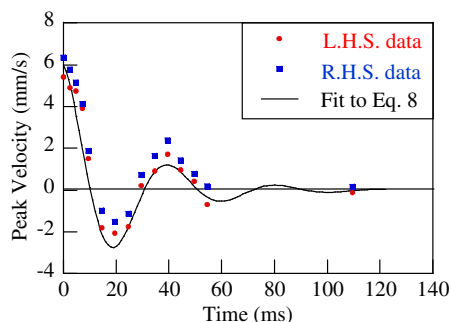


Fig. 9. Maximum velocity extracted from the left and right hand sides (L.H.S. and R.H.S.) of the Couette cell as a function of time following cessation of shear for the CPyCl/NaSal solution. The fit of Eq. (9) is also shown.

and phase) occurs over the imaging time, T (which in our implementation is ~ 25 ms). Any significant motion between pixels during T will result in significant image blurring. This was not a limitation for our implementation but would be problematic for significantly higher velocities or finer spatial resolutions (which would also necessarily increase T).

As with all EPI based pulse sequences, the ultimate temporal resolution that is achievable will be T_2^* limited whereas the number of sequential images that may be acquired will be T_2 limited. Ultimately these constraints will limit the range of liquids on which the rheological analysis performed here can be used. The most relevant MR technique to compare with is a velocity encoded RARE sequence [12–14]. Spatial resolution when applying RARE is T_2 limited. GERVAIS will acquire the required k -space data more rapidly; generally, however, RARE will offer better spatial resolution. The use of a CPMG (180° pulse) train in RARE results in a loss of quadrature, due to angle imperfections in the 180° refocusing pulses. Consequently at least two scans are typically required to restore velocity encoded phase information and as such the technique is not a single shot measurement and not suitable for acquisition of high temporal resolution data presented in Figs. 3–8. An innovative single shot RARE velocimetry technique has recently been developed [30]; its total acquisition time, however, makes it unsuitable for the transient flow fields considered here.

Manneville [31] reports the typical minimum acquisition time of velocity profiles inside rheometers as 2.5 ms for PIV, 10 ms for Dynamic Light Scattering (DLS) and 20 ms for Ultrasonic Velocimetry (USV). Our acquisition resolution (dictated by $\Delta = 3.1$ ms) is thus comparable to PIV when multiple repeats can be performed at variable times following some reproducible event (in our case the commencement or cessation of shear). The temporal resolution of our technique with respect to ‘steady state’ flow and the resolution of velocity fluctuations without a reference point is, however, $T = 25$ ms (T) and typically only for four temporal points. The temporal resolution for a large number of such points will be dictated by T_1 and be of the order of 1 s. Thus purely in terms of flexible application of acquisition speed, GERVAIS, does not compete with PIV, DLS and USV, except for the special case of event-triggered reproducible flow evolutions such as start up or decay. It does, however, not require optical access to the rheometer, is completely non-invasive (the fluid does not require to be seeded with scattering particles) and can be applied to opaque heterogeneous liquid solutions. This should ensure a relatively wide range of application.

7. Conclusions

This is the first application of GERVAIS, an ultrafast NMR velocity measurement technique, for the study of the evolution of the local velocity field in a complex fluid following start up or cessa-

tion of steady shear flow in a wide-gap Couette geometry. This is made possible by the novel inclusion of a variable delay time between a step change in imposed rotational velocity and the start of velocity encoding. The technique was applied to both a CPyCl/NaSal wormlike micellar solution and a viscous PDMS oil. Propagation of an elastic shear wave was observed for the CPyCl/NaSal solution following commencement of shear whilst an elastic recoil, resulting in reverse flow, was observed following the cessation of flow. Both are due to the viscoelastic nature of the fluid. Neither effect was observed for Newtonian PDMS indicating that these were real rheological responses and not equipment/methodology artefacts. Furthermore, the measured period of oscillation observed for the micellar solution was in excellent agreement with that calculated for an elastic shear wave, while the viscoelastic damping was stronger than expected for a linear Maxwell fluid. We suggest that this last observation may due to a finite stopping time of the inner cylinder or non-linear viscoelastic processes.

Acknowledgments

C.J.D. acknowledges funding from Unilever. Funding for A.J.S. and exchange visits for C.J.P. and M.L.J. from EPSRC Grant # GR/S20789/01 is also gratefully acknowledged.

References

- [1] E. Fukushima, Nuclear magnetic resonance as a tool to study flow, *Annu. Rev. Fluid Mech.* 31 (1999) 95–123.
- [2] P.T. Callaghan, Rheo-NMR and velocity imaging, *Curr. Opin. Colloid Interface Sci.* 11 (2006) 13–18.
- [3] T. Yamamoto, Numerical and experimental analyses of unsteady viscoelastic flow in complex flow field, *J. Soc. Rheol. Jpn.* 34 (2006) 283–289.
- [4] G.B. Bishko, O.G. Harlen, T.C.B. McLeish, T.M. Nicholson, Numerical simulation of the transient flow of branched polymer melts through a planar contraction using the ‘pom-pom’ model, *J. Non-Newtonian Fluid Mech.* 82 (1999) 255–273.
- [5] A.J. Sederman, M.D. Mantle, C. Buckley, L.F. Gladden, MRI technique for measurement of velocity vectors, acceleration, and autocorrelation functions in turbulent flow, *J. Magn. Reson.* 166 (2004) 182–189.
- [6] H. Rehage, H. Hoffman, Viscoelastic surfactant solutions – model systems for rheological research, *Mol. Phys.* 74 (5) (1991) 933–973.
- [7] M.M. Britton, P.T. Callaghan, Two-phase shear band structures at uniform stress, *Phys. Rev. Lett.* 78 (1997) 4930–4933.
- [8] P.T. Callaghan, A.M. Gil, H-1 NMR spectroscopy of polymers under shear and extensional flow, *Rheol. Acta* 38 (1999) 528–536.
- [9] P. Coussot, J.S. Raynaud, F. Bertrand, P. Moucheron, J.P. Guilbaud, H.T. Huynh, S. Jarny, D. Lesueur, Coexistence of liquid and solid phases in flowing soft-glassy materials, *Phys. Rev. Lett.* 88 (2002).
- [10] J.S. Raynaud, P. Moucheron, J.C. Baudez, F. Bertrand, J.P. Guilbaud, P. Coussot, Direct determination by nuclear magnetic resonance of the thixotropic and yielding behavior of suspensions, *J. Rheol.* 46 (2002) 709–732.
- [11] M.M. Britton, P.T. Callaghan, Shear banding instability in wormlike micellar solutions, *Eur. Phys. J. B* 7 (1999) 237–249.
- [12] W.M. Holmes, M.R. Lopez-Gonzalez, P.T. Callaghan, Fluctuations in shear banded flow seen by NMR velocimetry, *Europhys. Lett.* 64 (2) (2003) 274–280.
- [13] M.R. Lopez-Gonzalez, W.M. Holmes, P.T. Callaghan, Rheo-NMR phenomena of wormlike micelles, *Soft Matter* 2 (2006) 855–869.
- [14] S. Ahola, J. Perlo, F. Casanova, S. Stapf, B. Blumich, Multiecho sequence for velocity imaging in inhomogeneous rf fields, *J. Magn. Reson.* 182 (2006) 143–151.
- [15] I. Sersa, Auxiliary phase encoding in multi spin-echo sequences: application to rapid current density imaging, *J. Magn. Reson.* 190 (2008) 86–94.
- [16] K. Kose, Visualisation of turbulent motion using echo-planar imaging with a spatial tagging sequence, *J. Magn. Reson.* 98 (1992) 599–603.
- [17] K. Kose, Visualisation of local shearing motion in turbulent fluids using echo planar imaging, *J. Magn. Reson.* 96 (1992) 596–603.
- [18] M.C. Sains, M.S. El-Bachir, A.J. Sederman, L.F. Gladden, Rapid imaging of fluid flow patterns in a narrow packed bed using MRI, *Magn. Reson. Imaging* 23 (2005) 391–393.
- [19] M.C. Rogers, M.D. Mantle, A.J. Sederman, S.W. Morris, Conduits of steady-state autocatalytic plumes, *Phys. Rev. E* 77 (2008) 2.
- [20] P.T. Callaghan, Rheo-NMR: nuclear magnetic resonance and the rheology of complex fluids, *Rep. Prog. Phys.* 62 (4) (1999) 599–670.
- [21] K.G. Hollingsworth, M.L. Johns, Rheo-NMR of emulsion systems, *J. Rheol.* 48 (2004) 787–803.

- 562 [22] J.F. Berret, D.C. Roux, G. Porte, Isotropic-to-nematic transitions in wormlike
563 micelles under shear, *J. Phys. II Fr.* 4 (8) (1994) 1261–1279. 573
- 564 [23] A. Bhardwaj, E. Miller, J.P. Rothstein, Filament stretching and capillary breakup
565 extensional rheology measurements of viscoelastic wormlike micelle
566 solutions, *J. Rheol.* 51 (4) (2007) 693–719. 574
- 567 [24] C.J. Pipe, N.J. Kim, G.H. McKinley, The steady and transient non-linear rheology
568 of wormlike micellar solutions, Society of Rheology Annual Meeting, Journal of
569 Rheology, Maine, Portland, 2006. 575
- 570 [25] E. Miller, J.P. Rothstein, Transient evolution of shear-banding wormlike
571 micellar solutions, *J. Non-Newtonian Fluid Mech.* 143 (2007) 22–37. 576
- 572 [26] G.K. Batchelor, *An introduction to fluid dynamics*, CUP, 1973. 577
- [27] J.S. Lee, G.G. Fuller, Shear-wave propagation after stepwise increase of shear
rate, *J. Non-Newtonian Fluid Mech.* 39 (1) (1991) 1–15. 578
- [28] H.H. Hu, D.D. Joseph, Numerical-simulation of visco-elastic flow past a
cylinder, *J. Non-Newtonian Fluid Mech.* 37 (2–3) (1990) 347–377. 579
- [29] M.M. Denn, K.C. Porteous, Elastic effects in flow of viscoelastic liquids, *Chem.*
Eng. J. 2 (1971) 280–286. 580
- [30] A. Amar, F. Casanova, B. Blumich, Velocity maps measured in a single echo
using multi-echoes with independent encoding, O-15, 9th MRPM, Cambridge,
USA, 2008. 581
- [31] S. Manneville, Recent experimental probes of shear banding, *Rheol. Acta* 47
(2008) 301–318. 582
583
584

UNCORRECTED PROOF